MANCHESTER 1824
The University of Manchester

The University of Manchester Research

Modelling dynamic precipitation in pre-aged aluminium alloys under warm forming conditions

DOI:
10.1016/j.actamat.2022.118036

Document Version
Final published version

Link to publication record in Manchester Research Explorer

Citation for published version (APA):
Bignon, M., Shanthraj, P., & Robson, J. D. (2022). Modelling dynamic precipitation in pre-aged aluminium alloys under warm forming conditions. *Acta Materialia*, *234*, [118036]. https://doi.org/10.1016/j.actamat.2022.118036

Published in:
Acta Materialia

Citing this paper
Please note that where the full-text provided on Manchester Research Explorer is the Author Accepted Manuscript or Proof version this may differ from the final Published version. If citing, it is advised that you check and use the publisher's definitive version.

General rights
Copyright and moral rights for the publications made accessible in the Research Explorer are retained by the authors and/or other copyright owners and it is a condition of accessing publications that users recognise and abide by the legal requirements associated with these rights.

Takedown policy
If you believe that this document breaches copyright please refer to the University of Manchester's Takedown Procedures [http://man.ac.uk/04Y6Bo] or contact uml.scholarlycommunications@manchester.ac.uk providing relevant details, so we can investigate your claim.

OPEN ACCESS

Download date:21. Oct. 2022

Acta Materialia 234 (2022) 118036

Contents lists available at ScienceDirect

Acta Materialia

journal homepage: www.elsevier.com/locate/actamat

Modelling dynamic precipitation in pre-aged aluminium alloys under warm forming conditions

Madeleine Bignon*, Pratheek Shanthraj, Joseph D. Robson

Henry Royce Institute for Advanced Materials, The University of Manchester, Manchester M193PL, UK

ARTICLE INFO

Article history:
Received 4 March 2022
Revised 11 May 2022
Accepted 14 May 2022
Available online 18 May 2022

Keywords:
Dynamic precipitation
Aluminium alloys
Age-hardening
Excess vacancies
Warm forming

ABSTRACT

This work presents a model for deformation enhanced precipitate growth and coarsening kinetics in pre-aged 7xxx aluminium alloys under warm forming conditions (100 to 200 °C). A multi-class Kampmann–Wagner framework is used to describe the evolution of precipitate size distribution, where the effect of deformation is incorporated through enhanced solute diffusivity resulting from deformation induced excess vacancies. A classical phenomenological model is used to describe the accumulation of excess vacancies. The model is validated with experimental warm deformation data from the literature, and applied to investigate a wide range of deformation conditions to predict the effect of strain, strain rate and temperature on precipitate growth and coarsening kinetics. It is demonstrated that the interaction of solute supersaturation and excess vacancy concentration can lead to complex non-monotonic precipitate growth rate variation for certain regimes of strain rate and temperature.

© 2022 The Author(s). Published by Elsevier Ltd on behalf of Acta Materialia Inc.
This is an open access article under the CC BY license (http://creativecommons.org/licenses/by/4.0/)

1. Introduction

Precipitation is exploited to achieve good mechanical properties in aluminium alloys. The nucleation and growth of strengthening precipitates usually occur during a static heat treatment that does not involve any deformation. On the other hand, it is well-known that deformation significantly accelerates precipitation [1–7]. Therefore, operating the ageing treatment under deformation appears as a promising route to reduce the heat treatment duration. Furthermore, it may allow the development of novel precipitate distributions that gives desirable property combinations not possible to achieve by heat treatment alone. This strategy has been experimentally investigated under warm-forming conditions in pre-aged aluminium alloys from the 7xxx series [3,5,7–9]. The pre-ageing operation, typically performed around 100 °C, allows precipitates to nucleate and leaves the matrix in a supersaturated state, so that enough solute elements remain available for further precipitation. During subsequent warm forming at higher temperature (100 to 200 °C) the precipitates will evolve further towards the size which gives maximum (T6 equivalent) strength. However, it is not currently possible to predict this evolution, which means that the forming conditions are not optimised to give the best final precipitate distribution. A predictive model that addresses this problem is a key aim of the present work.

Precipitation under deformation, known as dynamic precipitation, is a complex phenomenon that has been the focus of multiple studies [3–5,7,10,11]. The mechanisms involved in the accelerating effect of deformation on precipitation include heterogeneous nucleation on dislocations [12,13], diffusionless solute dragging by dislocations ("ballistic transport") [12], pipe diffusion along dislocations [14,15] and deformation induced excess vacancies [15,16]. In pre-aged microstructures, nucleation is not expected to take place, and under warm forming conditions, both solute dragging and pipe diffusion appear negligible compared to the enhanced diffusion caused by the presence of vacancies [16]. As a result, precipitation acceleration during warm forming of pre-aged samples is mainly caused by the production of excess vacancies.

The kinetics of precipitation in the absence of deformation can be predicted using models relying on nucleation and growth equations, as demonstrated for instance in Robson et al. [13], Nicolas and Deschamps [17], Wagner et al. [18], Zhao et al. [19], Simar et al. [20], Porter et al. [21], Bardel et al. [22], Deschamps and Hutchinson [23]. Moreover, simple phenomenological models have proved capable of describing the evolution of vacancies during deformation [24–30], and the effect of strain-induced vacancies on diffusivity in aluminium alloys has been analysed and discussed before [16]. However, the calculation of the concentration of excess vacancies is not sufficient to predict the precipitation acceler-

* Corresponding author.
E-mail address: madeleine.bignon@manchester.ac.uk (M. Bignon).

https://doi.org/10.1016/j.actamat.2022.118036
1359-6454/© 2022 The Author(s). Published by Elsevier Ltd on behalf of Acta Materialia Inc. This is an open access article under the CC BY license (http://creativecommons.org/licenses/by/4.0/)

ation due to deformation. Indeed, the precipitation rate not only depends on the diffusivity, but also on the precipitate size distribution, and on the continuously changing solute supersaturation in the matrix. This paper present a novel model that enables dynamic precipitate evolution of a pre-tempered material under warm forming conditions to be predicted for the first time. The model is applied to precipitate evolution in 7xxx aluminim alloys and used to demonstrate the complex interactions between deformation and supersaturation on dynamic precipitate growth and coarsening. The implications of these dynamic effects in designing process paths to achieve a precipitate distribution to give maximum (T6 equivalent) strengthening are discussed.

2. The model

2.1. Outline

The aim of the model is to predict the time evolution of the precipitate size distribution, volume fraction and number density during deformation of a pre-aged microstructure as a function of the process parameters and initial distribution. The model is calibrated with and applied to the A7449 alloy of the Al-Zn-Mg system. The Kampmann and Wagner N-model (KWN model) [18] is used to describe the growth and coarsening of a pre-existing distribution and modified to account for the effect of deformation. The choice of the KWN framework for the kinetic part of the model is motivated by the fact that, as opposed to more simple and rapid models that describe the mean radius of the precipitates, it can predict the evolution of the full size distribution during the transformation. It has been shown that such a "multi-class" approach is necessary to correctly describe the transformation in the case of a pre-existing distribution [31]. The deformation is considered by modifying the diffusion coefficient to account for the production of excess vacancies [16]. The essential features of the model used in the present work are as follows:

- A microstructure with a pre-existing distribution of underaged precipitates is considered. The initial volume fraction, average radius and size distribution of this microstructure are inputs of the model, and the initial distribution is assumed to follow a log-normal law.
- The continuous precipitate size distribution is discretised in size classes. Each element of the class defines an average radius and is characterised by the number density of particles it contains.
- The continuous time evolution of the particle size distribution, of the concentration of excess vacancies and of the dislocation density is discretised. An auto-adaptative time step is used [31].
- At the end of each time-increment, the precipitate volume fraction is calculated by summing the contribution from each size class. The remaining amount of solute in the matrix is then updated considering the composition of the precipitates as constant.
- The interfacial energy of the precipitates is a calibration parameter in the model, fitted by matching experiment and prediction for the non-deformed case. The same interfacial energy is assumed to apply in the case of deformation.
- At each time step, the growth rate is calculated in each size class as outlined below. Depending on the sign of the growth rate, the particles of a size class are sent to the neighbouring class of upper size (positive growth rate) or lower size (negative growth rate). The influence of the particle radius on the interfacial composition (Gibbs Thomson effect) is taken into account.
- At each time increment, the concentration of excess vacancies resulting from deformation is calculated depending on temperature and strain rate using the vacancy evolution model described below. The effect of the excess vacancies on precipitate growth and coarsening is accounted for via the calculation of an effective diffusion coefficient that linearly depends on the amount of excess vacancies.
- The evolution of the concentration of excess vacancies is described using a classical model involving a production term proportional to the external mechanical work and an annihilation term that linearly depends on the dislocation density. The dislocation density is considered to have reached steady state; this assumption will be justified later.
- As has been demonstrated elsewhere [16], the contribution from enhanced diffusion along dislocations (pipe diffusion) is negligible for the conditions of interest here and was ignored to simplify interpretation of the model.

More details on the KWN model can be found elsewhere [18,31,32].

2.2. Growth and coarsening kinetics

2.2.1. Hypothesis on precipitation composition

The alloy considered throughout this work is A7449, with composition 8.3% Zn, 2.2% Mg, and 1.9% Cu (in wt.%) [3]. The precipitates usually identified in the Al-Zn-Mg system in the pre-aged condition are the metastable η' phase [3,9,17]. The precipitate composition is an important input parameter of any kinetic model, yet there is no general agreement on that of η' in the system considered here [33,34]. We adopt here the composition obtained with the Calphad method using the thermodynamic database TCAL8© and Thermocalc© software, which considers η' as a stoichiometric component of formulation $Mg_5Zn_7Al_6$. The composition of the precipitates is considered as constant.

2.2.2. Initial state

An initial existing precipitate distribution is considered, where the supersaturation is sufficiently low for nucleation to be ignored. The initial microstructure is defined by the initial distribution function $f^0(r)$ and volume fraction v_f^0. The initial distribution is assumed to follow a log-normal law, as it corresponds to the most frequently experimentally reported distribution [19,31,35]. Under this assumption, the distribution function is defined by two parameters, namely the initial mean radius $\bar{r}_0$ and dispersion parameter s, as Zhao et al. [19]:

$$f^0(r) = \frac{1}{\sqrt{2\pi}sr} \exp -\frac{1}{2s^2}\left(\ln(\frac{r}{\bar{r}_0}) + \frac{s^2}{2}\right)^2 \tag{1}$$

The initial volume fraction v_f^0 is an input of the model, from which the initial number density of precipitates N_0 (in particles per m^3) is determined as:

$$N_0 = v_f^0 \frac{\int_0^\infty f^0(r)dr}{\int_0^\infty f^0(r)\frac{4}{3}\pi r^3 dr} \tag{2}$$

The initial composition of the matrix depends on the initial volume fraction in the pre-aged microstructure and is determined as:

$$\bar{x}_i(t=0) = \frac{x_i^0 - v_f^0 \cdot x_i^{pr}}{1 - v_f^0} \tag{3}$$

where i designates Mg or Zn, x_i^{pr} is the atomic concentration in i in the precipitate, and x_i^0 is the bulk concentration in i in the matrix.

2.2.3. Thermodynamics

Modelling precipitation kinetics requires a prediction of the local equilibrium conditions at the particle/matrix interface as a

Table 1
Model constants and ranges of values from the literature.

Symbol	Parameter	Adopted value	Reference
D_0	Prefactor for solute diffusion	1.49×10^{-5} m^2/s	(0.63 to 12)$\times 10^{-5}$ m^2/s [41]
Q	Solute migration energy	115.9 kJ/mol	112.1 to 161.1 kJ/mol [41]
D_0^v	Prefactor for vacancy diffusion	1.0×10^{-5} m^2/s	[16]
Q_m	Vacancy migration energy	0.93 eV	0.58 to 1.0 eV [16,40]
Q_f	Vacancy formation energy	0.52 eV	0.52 to 0.76 eV [27,39,42,43]
Q_j	Jog formation energy	0.3 eV	[16]
ΔH	Enthalpy of precipitation	302.6 kJ/mol	–
ΔS	Entropy of precipitation	84.1 J/mol/K	–
κ	Dislocation arrangement constant	10	1 to 10 [26]
χ	Mechanical vacancy production term	0.035	0.01 to 0.1 [26,27]
ξ	Thermal jog vacancy production term	0.5	[26]
γ	Interfacial energy	180 mJ/m^2	50 to 400 mJ/^{2} [17,19,22,44–46]
Zn/Mg	Zn/Mg in precipitates	1.4	1 to 2.2 [47]
Zn/(Mg + Al)	Zn/(Mg + Al) in precipitates	0.64	0.66 to 1.82 [34,48]
v_{at}^{pr}	Atomic volume of the precipitate	1.66×10^{-19} m^3	
Ω_0	Atomic volume of the matrix	1.66×10^{-19} m^3	[16]
Q^σ	Activation energy in the flow stress law	60 kJ/mol	[38]
n	Exponent in the flow stress law	6.683	[38]
A	Constant in the flow stress law	5.214×10^6 s^{-1}	[38]
α	Constant in the flow stress law	5.57×10^{-3} MPa^{-1}	–

function of composition and temperature. A convenient way to achieve this is to use the dilute solution assumption, and a solubility product, as suggested by Nicolas et al. [17]. The molar concentrations x^∞_{Mg} and x^∞_{Zn} of a matrix in equilibrium with a precipitate $Mg_5Zn_7Al_6$ are related to the solubility product K^∞ by:

$$K^\infty = (x^\infty_{Mg})^5 \cdot (x^\infty_{Zn})^7 \cdot (x^\infty_{Al})^6 \approx (x^\infty_{Mg})^5 \cdot (x^\infty_{Zn})^7 \tag{4}$$

with

$$K^\infty(T) = \exp\left(\frac{\Delta S}{R} - \frac{\Delta H}{RT}\right) \tag{5}$$

where ΔS and ΔH are respectively the entropy and enthalpy associated with the precipitate formation [17]. In this work, x^∞_{Mg} and x^∞_{Zn} were calculated for AA7449 [3] at different temperatures with the thermodynamic database TCAL8©, by supressing all phases except for the face centered cubic matrix phase and the η' precipitate. These values were used to calculate K^∞ at different temperatures using Eq. (4) and the entropy and enthalpy were identified by linear regression with Eq. (5). The obtained values are shown in Table 1.

Additionally, the reaction is considered to be stoichiometric so that:

$$7 \cdot (x^0_{Mg} - x^\infty_{Mg}) = 5 \cdot (x^0_{Zn} - x^\infty_{Zn}) \tag{6}$$

where x^0_{Mg} and x^0_{Zn} are the bulk concentrations of Mg and Zn in the alloy. For a given mean alloy composition and a given temperature, Eqs. (4) and (6) define respectively the solvus line and the stoichiometric line, and the intersection of these lines determines the equilibrium [17].

2.2.4. Growth rate

Following classical precipitation models, the growth rate of a spherical precipitate of radius r is considered to be controlled by the slowest diffuser (here Mg [17]) and is calculated as:

$$\frac{dr}{dt} = \frac{D_{eff}}{r} \cdot \frac{\bar{x}_{Mg} - x^r_{Mg}}{x^{pr}_{Mg} - x^r_{Mg}} \tag{7}$$

where D_{eff} is the effective diffusion coefficient of Mg, which depends on deformation as detailed in Section 2.3; x^{pr}_{Mg} is the concentration of Mg in the precipitate, calculated as $5/18 = 0.28$; $\bar{x}_{Mg}$ is the average concentration of Mg in the matrix, that changes as the total volume fraction of precipitate changes; and x^r_{Mg} is the equilibrium concentration at the interface between the matrix and a precipitate of radius r. According to the Gibbs–Thomson effect, the curvature at the interface for a spherical particle results in an increase in the free energy compared to a flat interface, which results in an equilibrium concentration x^r_{Mg} different than x^∞_{Mg} [21].

In the case of a binary system, x^r can be straightforwardly deduced from x^∞ [21], but in a multicomponent system, its calculation becomes more complex. Following the analysis of Perez [36], who discusses the formulation of the Gibbs Thomson effect in the general case, the equilibrium concentrations at the interface between the matrix and a precipitate $Mg_5Zn_7Al_6$ depends on the radius r of the precipitate via:

$$\frac{2\gamma v^{pr}_{at}}{rkT} \cdot (5+7+6) = 5 \cdot \ln\frac{x^r_{Mg}}{x^\infty_{Mg}} + 7 \cdot \ln\frac{x^r_{Zn}}{x^\infty_{Zn}} + 6 \cdot \ln\frac{x^r_{Al}}{x^\infty_{Al}} \tag{8}$$

where γ is the interfacial energy of the precipitate and v^{pr}_{at} its atomic volume. This can be reformulated as:

$$\frac{2\gamma v^{pr}_{at}}{rkT} \cdot (5+7+6) = \ln\left(\frac{(x^r_{Mg})^5 \cdot (x^r_{Zn})^7 \cdot (x^r_{Al})^6}{(x^\infty_{Mg})^5 \cdot (x^\infty_{Zn})^7 \cdot (x^\infty_{Al})^6}\right) \tag{9}$$

so that the solubility product of a spherical interface K^r can be related to that of a flat interface K^∞ by:

$$K^r = K^\infty \exp\left(\frac{2\gamma v^{pr}_{at}}{rkT} \cdot (5+7+6)\right) \tag{10}$$

where

$$K^r = (x^r_{Mg})^5 \cdot (x^r_{Zn})^7 \cdot (x^r_{Al})^6 \approx (x^r_{Mg})^5 \cdot (x^r_{Zn})^7 \tag{11}$$

and the equilibrium concentrations x^r_{Mg} and x^r_{Zn} can then be calculated for any radius r as the intersection between the solvus line defined by Eq. (11) and the stoichiometric line defined by Nicolas and Deschamps [17]:

$$7 \cdot (x^0_{Mg} - x^r_{Mg}) = 5 \cdot (x^0_{Zn} - x^r_{Zn}) \tag{12}$$

At each time step, the new precipitate size distribution is determined by calculating the growth rate in each bin of the size distri-

bution, and reallocating the particles in the neighbouring bins as explained in Perez et al. [31].

2.2.5. Coarsening

During the precipitation process, the smallest particles tend to dissolve, releasing solute in the matrix and providing driving force for the largest particles to grow further; this is known as coarsening. One of the advantages of the KWN framework is that coarsening arises naturally in the model and no additional parameter needs to be added to describe it. The critical radius r^*, defined as the radius below which particles shrink can be calculated as the radius such that $\frac{dr}{dt} = 0$ using Eq. (7).

2.3. Effect of deformation on precipitation growth and coarsening

2.3.1. Enhancement of diffusion

When deformation takes place, excess vacancies are created due to the non-conservative motion of jogs on mobile screw dislocations [37]. This increases the mobility of the atoms, and thus enhances diffusion. The effect of excess vacancies can be accounted for by calculating an effective diffusion coefficient under deformation as Robson [16]:

$$D_{\text{eff}} = D_{\text{th}}\left(1 + \frac{c_{\text{ex}}}{c_{\text{th}}}\right) \tag{13}$$

where D_{th} is the diffusion coefficient without deformation, calculated in the usual way with the prefactor D_0 and the activation energy for solute migration Q, c_{ex} is the concentration of excess vacancies, calculated as outlined below, c_{th} is the equilibrium concentration of thermal vacancies, calculated as $c_{\text{th}} = 23\exp(\frac{-Q_f}{kT})$ [28], where Q_f is the vacancy formation energy. The effect of pipe diffusion is ignored, as it has been shown elsewhere that it is negligible in the range of temperatures considered here [16].

2.3.2. Time evolution of excess vacancies

The different models available in the literature (e.g. Robson [16], Lenasson [24], Mecking and Estrin [25], Militzer et al. [26], Detemple et al. [27], Linga Murty et al. [28]) describe the vacancy evolution as a balance between a production term - that depends on the external work - and an annihilation term, reflecting the tendency of vacancies to migrate towards sinks such as grain boundaries and dislocations [27]. Although these terms may slightly vary depending on the models [27], the philosophy of the different approaches is the same. The phenomenological model proposed by Militzer et al. [26] is used here. This model has been described and analysed elsewhere [16], and only the most important features are reproduced. The evolution of excess vacancies concentration during deformation is written as:

$$\frac{\mathrm{d}c_{\text{ex}}}{\mathrm{d}t} = \left(\chi\frac{\sigma\Omega_0}{Q_f} + \xi\frac{c_j\Omega_0}{4b^3}\right)\dot{\epsilon} - \left(\frac{\rho}{\kappa^2} + \frac{1}{L^2}\right)D_v c_{\text{ex}} \tag{14}$$

In Eq. (14), χ is a phenomenological constant that describes the fraction of mechanical work converted into vacancies during mechanical loading. The first term of Eq. (14) implicitly contains the density of mobile dislocations that produce the vacancies. The strain rate dependency comes from the fact that the production of vacancies $\mathrm{d}c_{\text{ex}}$ during a time increment dt is proportional to the increment in plastic work $\mathrm{d}W = \sigma\,\mathrm{d}\epsilon$, so that the vacancy production rate $\frac{\mathrm{d}c_{\text{ex}}}{\mathrm{d}t}$ is proportional to $\frac{\mathrm{d}W}{\mathrm{d}t} = \sigma\frac{\mathrm{d}\epsilon}{\mathrm{d}t}$. Ω_0 is the atomic volume of the matrix and b is the Burgers vector. c_j is the concentration of thermal jogs, calculated from the jog formation energy Q_j as $\exp(-\frac{Q_j}{kT})$. ξ is a parameter related to the contribution of thermal jogs to the production of excess vacancies. This term generally depends on the concentration of jogs, but can be considered as constant and equal to 0.5 for the range of temperatures considered here [26]. σ is the flow stress, which is strain rate and temperature dependent and is calculated here via a classical sinepowerlaw as:

$$\sigma = \frac{1}{\alpha}\cdot\operatorname{asinh}\left[\left(\frac{\dot{\epsilon}}{\mathrm{A}}\exp(\mathrm{Q}^{\sigma}/\mathrm{RT})\right)^{1/\mathrm{n}}\right] \tag{15}$$

where $n = 6.68309$ and $Q^{\sigma} = 60$ kJ/mol, which reflect respectively the strain rate and temperature sensitivity of the flow stress, are taken from measurements on A7449 in Wang et al. [38]; $A = 5.214\times10^{6}$ s^{-1} is a constant [38], and α is an empirical constant taken here as 5.57×10^{-3} mPa^{-1} to match the flow stress measured in Deschamps et al. [3].

In Eq. (14), ρ is the dislocation density, considered as having reached its saturation value and thus taken as constant; this simplifying assumption will be discussed later. The term κ is a phenomenological constant that describes how effective sinks the dislocations constitute, depending on their arrangement (homogeneous or cell structures), and L is the grain size. D_v is the diffusion coefficient of vacancies, equal to $D_0^v\exp(-\frac{Q_m}{kT})$, where Q_m is the activation energy for vacancy migration.

3. Model parameters

The model described above contains several physical parameters - some of which are only approximately known - as well as phenomenological constants. In the present work, these parameters have been calibrated for A7449, using the experimental in situ SAXS data from Deschamps et al. [3]. The comparisons between calculations and experimental results will be shown later.

The physical parameters of the model are often available in the literature but imprecisely defined. Whenever these parameters are ill-defined, their values were selected so as to reach acceptable agreement between calculations and experiments. The selected parameters are shown in Table 1 with the reference values from the literature. The value of 0.93 eV for Q_m, though large compared to the 0.75 eV measured in pure aluminium [39], is consistent with previous assessments from the literature for Al-Zn-Mg systems [3,16,40]. The chosen value of Q_f corresponds to the minimum value found in the literature. Further, the interfacial energy can usually not be directly measured, and a wide range of possible values appear in the literature. The interfacial energy as well as the vacancy migration and formation energies are adjustable parameters of the model, but it can be noted that the values selected here fall in a physically reasonable range compared to the ones found in the literature, as can be seen, along with the values of all parameters, in Table 1.

Though the selected values of Q_f, Q_m, and γ appear reasonable compared to other models or experimental data from the literature, not too much physical meaning should be drawn from them in the present work. Cautious interpretation of these values is even more necessary, considering that the set of parameters chosen here may not be unique, and that the fitting parameters mentioned before depend both on the enthalpy and entropy of precipitation, obtained from Thermocalc®, and on the assumed composition of the precipitate, which is not well established and might even vary during the transformation. However, since the ambition of this work is not to accurately calculate the values of physical constants, but rather to exploit a phenomenological model capturing the main features of precipitation under deformation, the non uniqueness of the set of model parameters is not a major issue. More pragmatically, the reasonable agreement obtained between available experimental data and calculations - discussed later - seems to justify the set of parameters selected here.

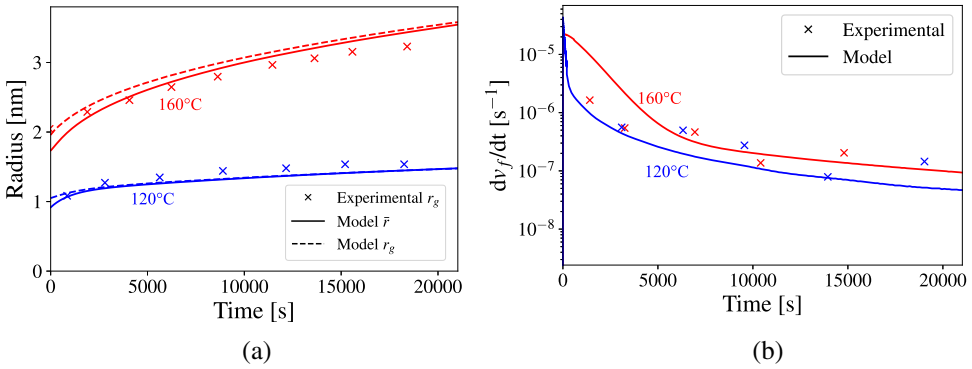

Fig. 1. Evolution of (a) the calculated mean and Guinier radii; (b) the change rate in the volume fraction as a function of time for the experimental conditions described in Deschamps et al. [3], Fribourg et al. [49] and comparison with experiments.

4. Results and discussion

4.1. Comparison with experiments

4.1.1. Static precipitation

The correctness of the kinetics part (without deformation) of the model is first demonstrated using experimental data from the literature, where the Guinier radius of the precipitates was measured as a function of time during isothermal heat treatment at 120 °C and 160 °C in A7449 [3,49].

The input parameters used for this calculation are shown in Table 2. At 160 °C, the initial mean radius $\bar{r}_0$ and the dispersion parameter s of the distribution were determined by fitting the distribution function of Eq. (1) to the Kratky plot provided in ref. [3] using the procedure outlined in Deschamps and De Geuser [35]. For the heat treatment at 120 °C, the only information regarding the initial distribution was the Guinier radius, so the initial dispersion parameter s was assumed to be the same as for the 160 °C heat treatment. The initial volume fraction v_f^0 is expressed here as a fraction of the equilibrium volume fraction at 160 °C (v_f^{eq} (160 °C)), because the experimentally determined volume fraction value depends on the assumption made on the precipitate composition, which is not the same in ref. [3] and in the present work.

The calculated time evolution of the mean radius $\bar{r}$ is shown in Fig. 1(a), along with the calculated Guinier radius r_g, estimated from the precipitate distribution as detailed in Deschamps and De Geuser [35]. Experimental Guinier radius measurements from the literature are displayed as well. Experimental Guinier radii and calculated mean radii must usually be compared cautiously since the Guinier radius of a precipitate distribution is not in general equal to the mean value of the precipitate size distribution [35]. As demonstrated in Deschamps and De Geuser [35], the relation between the Guinier radius and the mean radius of the precipitate distribution depends on the dispersion parameter s. In the case at hand, Fig. 1 shows that the mean and Guinier radii are fairly equivalent. Therefore, no further distinction will be made between Guinier radius and mean radius throughout this work. Fig. 1(b) also shows the calculated evolution of the change rate in the volume fraction with respect to time, along with the experimental values from the literature. The comparison between model and experiment is made on the change rate in the volume fraction and not on its absolute value for the reason mentioned above.

As can be seen in Fig. 1, both the calculated mean radius and the change rate in volume fraction during static heat treatment at 120 °C and 160 °C show reasonable agreement with experiment, sufficient to ensure that the effect of temperature alone on the precipitate evolution is correctly captured in the model.

Table 2
Inputs for calculation during static heat treatment.

T	$\bar{r}_0$	s	v_f^0/v_f^{eq} (160 °C)
120 °C	0.93 nm	0.25	0.54
160 °C	1.75 nm	0.25	0.82

4.1.2. Dynamic precipitation

The results obtained with the calibrated model for the case of dynamic precipitation are now compared with the experimental data of Deschamps et al. [3], where pre-aged samples were deformed at 160 °C with strain rates varying between 10^{-5} and 10^{-4}/s, and compared with non-deformed samples undergoing a static heat treatment at 160 °C. In this set of experiments, the deformed samples were maintained at high temperature after deformation. The time at which deformation stops is indicated by vertical dotted lines in Fig. 2. The input values are gathered in Table 3. Regarding the deformation conditions, the strain rate time evolution was linearly interpolated from the curves provided in Deschamps et al. [3], considering only the part of deformation in the plastic regime. The dislocation density is considered as constant and equal to 10^{14} m^{-2}, which is a typical saturation value for this alloy family [50]; this assumption will be discussed later. A grain size of 50 μm is assumed here as in Robson [16], but the model predictions are not very sensitive to the grain size value. It should be noted that the model could only be compared with experimental data for relatively low strain rates as these are the ones used in the set of experiments of Deschamps et al. [3], which is the only one of its kind available in the literature.

Fig. 2 (a) shows the calculated rate of increase in the mean radius with respect to time, together with the experimentally measured rate of increase in the Guinier radius from [3]. For the precipitation distributions considered here, the Guinier radius and mean radius are equivalent [3], and their rate can thus directly be compared. The filled areas represent the experimental uncertainty of ±0.15 pm/s in the growth rate measurement appearing in Deschamps et al. [3]. The evolution of growth rate with time as a function of deformation conditions will be discussed in more details later, but the qualitative shape of the growth rate under deformation apparent in Fig. 2(a) consists in (i) an initial decrease in the growth rate before the deformation starts, corresponding to a growth and coarsening regime; (ii) an increase in the growth rate during deformation, due to the production of excess vacancies; (iii) a decrease in the growth rate, starting when the deformation stops, again corresponding to a conventional growth and coarsening regime without any deformation. As can be seen in

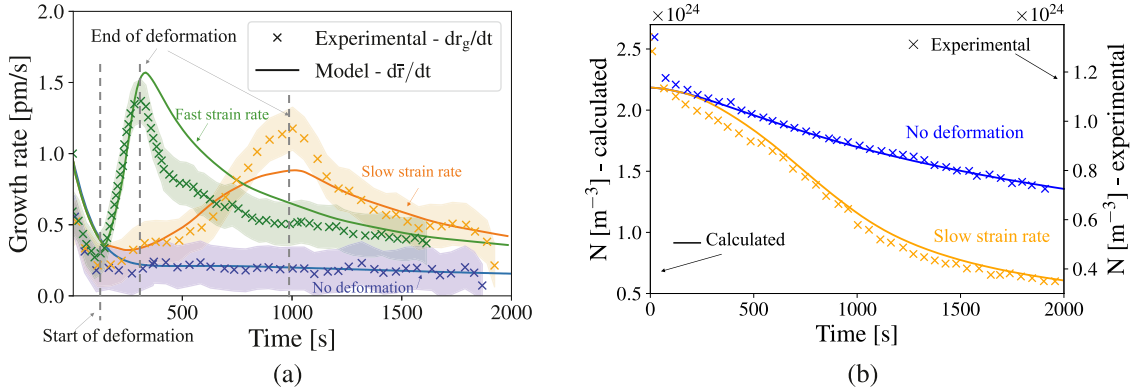

Fig. 2. (a) Growth rate as a function of time for the experimental conditions described in Deschamps et al. [3]. The plain lines are the values calculated with the models, the crosses are the experimental values from Deschamps et al. [3] and the filled areas show the experimental uncertainty, estimated to ±0.15 pm/s. The slow strain rate experiment corresponds to an approximate value of 5×10^{-5}/s while the fast one corresponds to a maximum of 5×10^{-4}/s. The vertical dotted lines show the time of the end of the deformation for the deformed samples. (b) Evolution of the calculated number density of precipitates (plain line and left hand side scale for the vertical axis), along with the experimental data from [3] (crosses and right hand side scale for the vertical axis).

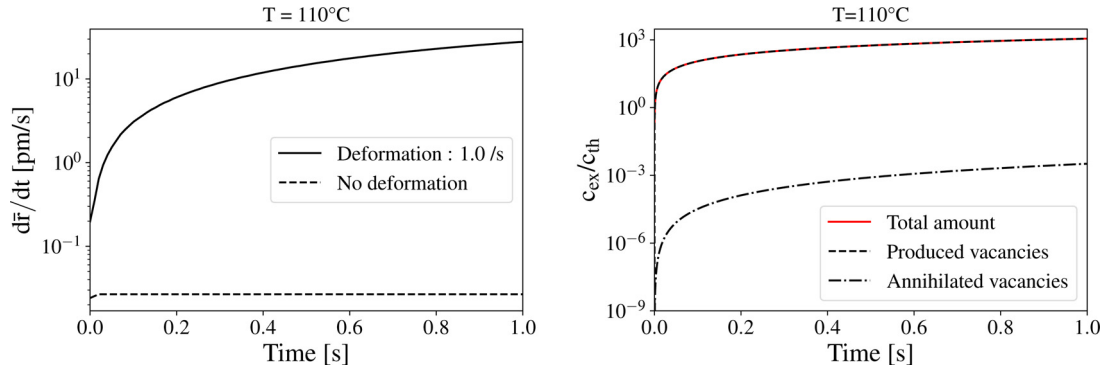

Fig. 3. a) Evolution of the growth rate as a function of time, with and without deformation to $\epsilon = 1$. b) Evolution of the total concentration of excess vacancies divided by the equilibrium concentration, under deformation with $\dot{\epsilon} = 1$/s, showing the accumulated number of vacancies produced during deformation, and the accumulated number of vacancies that have been annihilated (with a negative sign to account for their negative contribution to the total number of vacancies).

Fig. 2(a), fair agreement is obtained for the precipitation growth rate under deformation at fast strain rate. Higher differences are observed for the growth rate under slower strain rate, where the calculated maximal growth rate is lower than the one experimentally reported. However, the trends regarding the ranking of the maximum growth rates with respect to deformation rate are captured by the model, as can be seen in Fig. 2(a), and the level of fit reached here therefore appears reasonable.

The calculated evolution of the number density of precipitates is shown in Fig. 2(b) along with the experimental values from [3] for the case without deformation and with deformation at slow strain rate. The case with deformation at fast strain rate is not shown as the experimental values were not available in the literature. It should be noted that the experimental and calculated values are not displayed with the same scale for the vertical axis. This is because, as mentioned before, the experimental values obtained from SAXS measurements for the volume fraction or number density of precipitates are only relative, and the determination of their absolute values requires a calculation that involves hypotheses on the composition. It can nevertheless be observed from Fig. 2 (b) that the calculated evolution of the number density of precipitates is very similar to the experimental values in terms of trends.

4.2. Application of the model: accelerating effect of dynamic ageing compared to static ageing

In order to estimate the accelerating effect of deformation on precipitation, it is first useful to compare the precipitate growth rates with and without deformation under different deformation conditions. The other input parameters are the same as in Table 3.

4.2.1. Relatively low temperature and high strain rate

The calculated growth rate under deformation at relatively low temperature (110 °C) and high strain rate ($\dot{\epsilon} = 1$/s) is shown in Fig. 3(a), along with the calculated growth rate during an equivalent time without any deformation. Under these conditions, deformation considerably accelerates precipitate growth rate with an up to 1000 fold increase compared to the case without deformation. This can be explained by the amount of excess vacancies produced during deformation, as shown in Fig. 3(b). The high strain rate allows a high excess vacancies production rate (Eq. (14)), while the relatively low temperature limits the vacancy mobility, so that vacancy annihilation is almost negligible (Eq. (14)). This results in a constantly increasing amount of excess vacancies during deformation, and thus in a significant enhancement of precipitate growth compared to the non-deformed case.

4.2.2. Relatively high temperature and low strain rate

The calculated growth rate under deformation at higher temperature (200 °C) and low strain rate ($\dot{\epsilon} = 10^{-4}$/s) is shown in Fig. 4(a), along with the calculated growth rate during an equivalent time without any deformation. Under these conditions, deformation still accelerates precipitation, as apparent in Fig. 4(a), but to a much lower extent compared to the case of a lower temperature and higher strain rate. In turn, at 200 °C and for $\dot{\epsilon} = 10^{-4}$/s, the maximal amount of produced excess vacancies is relatively low

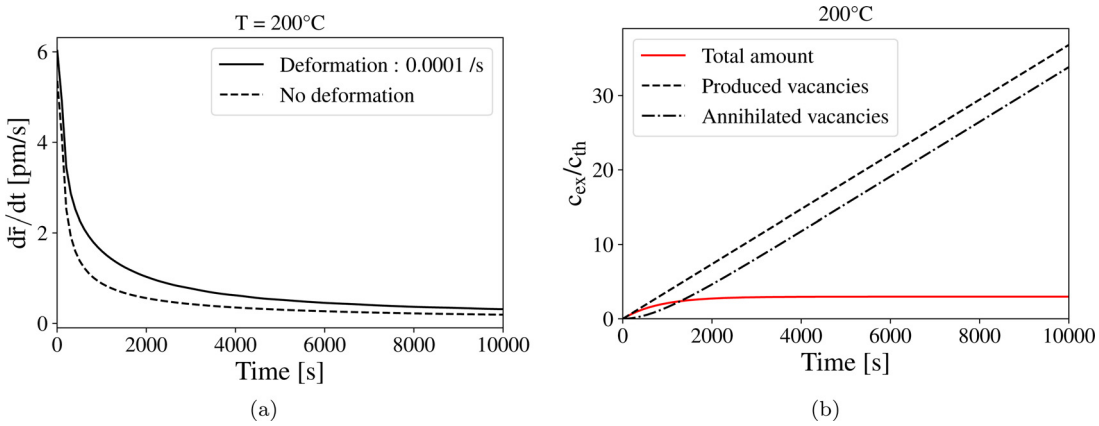

Fig. 4. a) Evolution of the growth rate as a function of time, with and without deformation to $\epsilon = 1$. b) Evolution of the total concentration of excess vacancies divided by the equilibrium concentration, under deformation with $\dot{\epsilon} = 10^{-4}$/s, showing the accumulated number of vacancies produced during deformation, and the accumulated number of vacancies that have been annihilated.

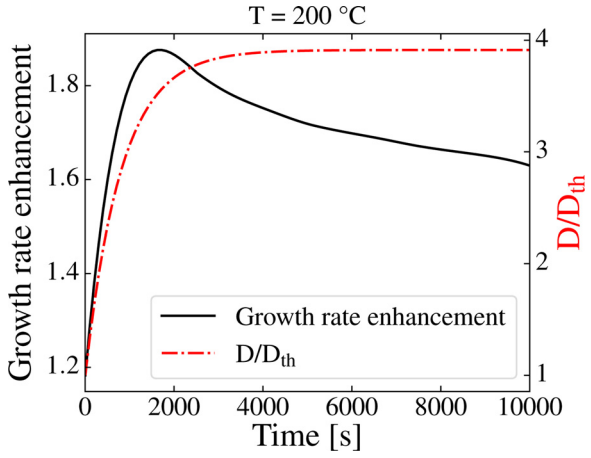

Fig. 5. Growth rate enhancement as a function of time, defined as the calculated dr̄/dt under deformation at $\dot{\epsilon} = 10^{-4}$/s and 200 °C divided by dr̄/dt without any deformation; along with the evolution of the ratio D/D_{th}, which is the diffusion coefficient under deformation divided by the diffusion coefficient without any deformation.

(Fig. 4(b)). As a matter of comparison, the maximal value of the ratio c_{ex}/c_{th} is around 300 times higher for the lower temperature and higher strain rate considered in Fig. 3(b) than for the higher temperature and lower strain rate considered in Fig. 4(b). This is because in the second case, the low strain rate produces only a low amount of excess vacancies (Eq. (14)). Further, because of the higher temperature, vacancies are more mobile and can easily annihilate at sinks such as dislocations as shown in Fig. 4(b). As a result, the excess vacancies concentration reaches a low saturation value at the early stage of deformation and the accelerating effect of deformation is limited.

To understand better the role played by deformation in the evolution of dr̄/dt, Fig. 5 shows the calculated evolution of the growth rate under deformation divided by the growth rate without any deformation, together with the ratio D/D_{th}, which shows the diffusivity enhancement caused by deformation. It might be surprising to see that, whereas the diffusivity is multiplied by 4 by deformation, the growth rate only shows a maximum of 1.8-fold increase compared to the non deformed case. This is because the growth rate of a given precipitate is not solely controlled by the diffusivity, but also by the concentration gradient from the precipitate to the matrix and by its radius (Eq. (7)). This can be seen by plotting the supersaturation, taken here for a precipitate with flat interface, and defined as $\frac{\bar{x}_{Mg} - x^{eq}_{Mg}}{x^{pr}_{Mg} - x^{eq}_{Mg}}$, both for the deformed and non deformed case as in Fig. 6(a). The initial increase in the growth rate due to deformation (Fig. 5) results in a faster initial decrease of the supersaturation level compared to the non-deformed case, as shown in Fig. 6(a). This accelerated decay in supersaturation partly reduces the growth acceleration due to enhanced diffusivity. Further, since the initial growth rate is higher under deformation, the mean radius becomes larger (Fig. 6(b)) than without deformation, and the growth rate is thus lower than would be expected considering only the enhancement of the diffusivity. This shows that the enhancement in growth rate cannot in general be deduced from the amount of excess vacancies alone, and emphasises the importance of embedding the deformation induced excess vacancies model in a kinetics framework.

4.2.3. Intermediate temperature and strain rate - example of a more complex behaviour

For intermediate temperature and strain rate, for instance 150 °C and $\dot{\epsilon} = 0.01$/s, the calculated growth rate shows more complex behaviour, with a non monotonic evolution, as apparent in Fig. 7(a). In that case, the excess vacancies concentration, which increases constantly and almost linearly with time, is not sufficient to fully explain the evolution of the growth rate, as shown in Fig. 8(a).

The initial shape of the growth rate curve can be better explained by considering the main terms involved in the growth rate (Eq. (7)), i.e. the evolution of the supersaturation and the diffusion coefficient, or, in the present case, its ratio compared to the diffusion coefficient without any deformation D_{th}. These quantities and their time derivative are drawn in Fig. 8(c) and (d), respectively, with the times t_1 and t_2 which correspond to the times of the minimum and maximum reached by the growth rate. At the beginning of the deformation ($t < t_1$), the growth rate increases (Fig. 8(a)) because the supersaturation is dropping less sharply than the excess vacancies concentration is increasing (Fig. 8(c) and (d)). As precipitates grow and coarsen, the supersaturation decreases, and its decay becomes faster as the growth rate increases. At the critical time t_1, the rate of decrease of the supersaturation (Fig. 8(d)) overwhelms the accelerating effect of enhanced diffusion, and the growth rate starts decreasing.

At t_2, dr̄/dt reaches a minimum. This minimum corresponds to the start of a coarsening dominated regime, as can be seen in Fig. 8(b), where the volume fraction and precipitate number den-

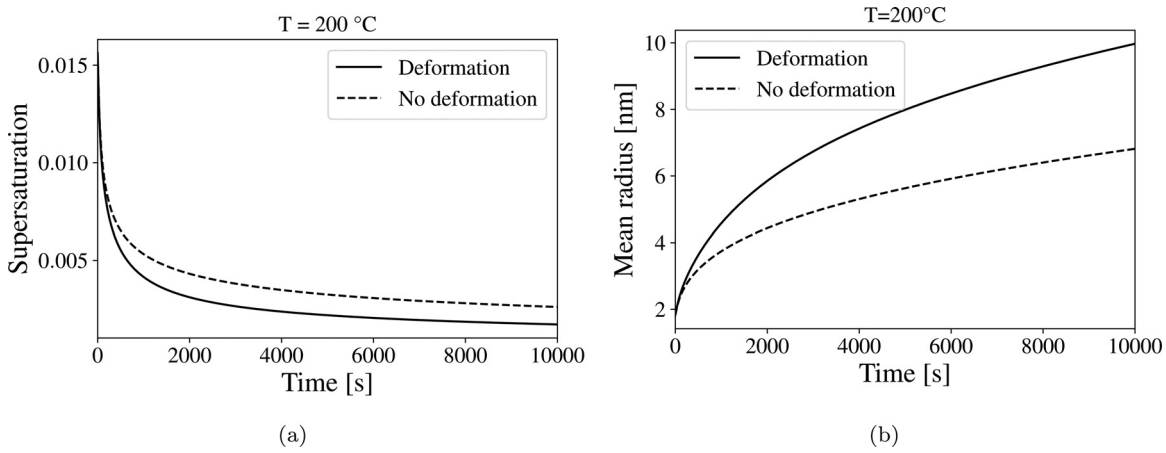

Fig. 6. a) Evolution of the supersaturation as a function of time, with and without deformation to $\epsilon = 1$. b) Evolution of the supersaturation as a function of time, with and without deformation to $\epsilon = 1$. The calculations are made for deformation with $\dot{\epsilon} = 10^{-4}$/s and 200 °C.

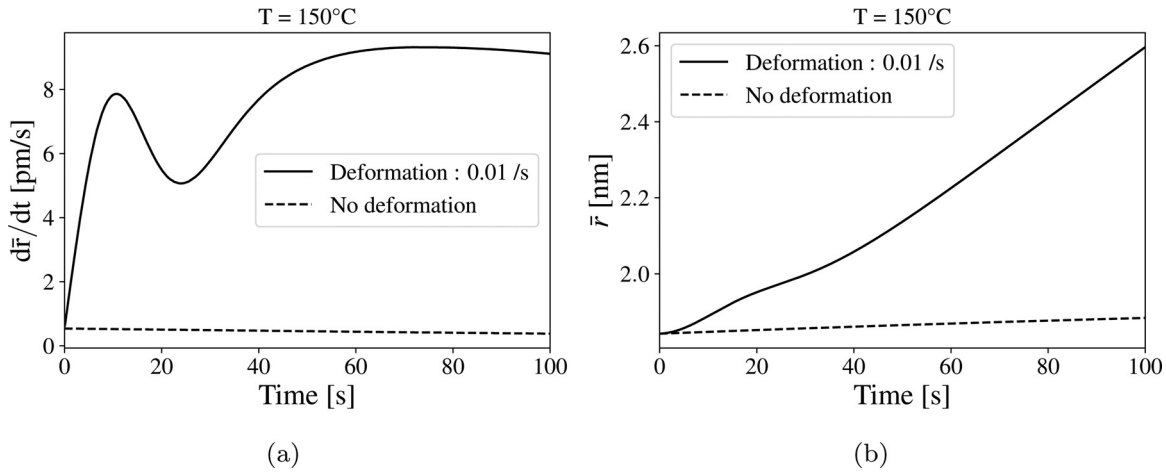

Fig. 7. Evolution of (a) the growth rate and (b) the mean radius as a function of time; with and without deformation to $\epsilon = 1$ with $\dot{\epsilon} = 0.01$/s.

sity are shown as a function of time. From t_2, the smallest particles dissolve faster and faster, resulting in an accelerated decrease in the number of precipitates, and the solute released in the matrix by the dissolution of the smallest precipitates is consumed by the growth of the largest precipitates, so that the average radius increases while the supersaturation remains nearly constant (Fig. 8(b)). As opposed to coarsening during static ageing, where the average growth rate continuously decreases with a $D/\bar{r}^2$ dependency [21], $d\bar{r}/dt$ increases during coarsening under deformation for the temperature and strain rate considered here. Since the supersaturation level varies little after t_2, the growth rate evolution law is mainly a competition between the increasing diffusion coefficient - that accelerates coarsening - and the increasing average radius - which reduces the growth rate. In the case at hand, the continuously increasing diffusion coefficient (Fig. 8(c) and (d)) due to the production of excess vacancies is sufficient to cause an initial increase in $d\bar{r}/dt$ after t_2, which becomes less and less sharp as the mean radius increases (Fig. 7(b)). Finally $d\bar{r}/dt$ stabilises when its value is sufficiently high so that the rate of increase of $\bar{r}$ in Eq. (7) compensates the rate of increase in D, in such a way that $d\bar{r}/dt$ starts a slow decrease.

4.3. Influence of processing parameters on dynamic precipitation

In order to estimate the effect of deformation conditions on dynamic precipitation, the precipitation rates obtained under various conditions are compared. The model is applied to different strains, strain rates and temperatures, and the other input parameters are the same as in Section 4.2.

4.3.1. Influence of strain rate and strain

The precipitation rate depends on strain rate, as can be seen in Fig. 9, where the calculated precipitate growth rate with respect to time ($\frac{d\bar{r}}{dt}$) is plotted as a function of strain for various strain rates at 120 °C (Fig. 9(a)) and 180 °C (Fig. 9(b)). It should be noted that for a same level of strain, the total precipitation duration is different since the different lines correspond to different strain rates.

It can first be noted from Fig. 9(a) and (b), that for both temperatures, $\frac{d\bar{r}}{dt}$ increases fairly linearly with strain at the initial stage of deformation and shows little dependency to strain rate. As strain increases however, the trend changes, and, while the growth rate keeps increasing with strain for high strain rates (10^{-2} and 10^{-1} s^{-1}), it reaches a maximum for lower strain rates. The two examples from Fig. 9 show that the strain rate sensitivity of the precipitation rate is not monotonic and varies depending on the ranges of temperature, strain and strain rate under consideration. These calculations may help explaining contradictory experimental results found in the literature, where the precipitation rate has been reported to show positive sensitivity [7], negative sensitivity [5,10] or no sensitivity [3] to strain rate.

4.3.2. Processing maps

The model has a practical interest as it can be used to determine the deformation conditions necessary to reach a certain pre-

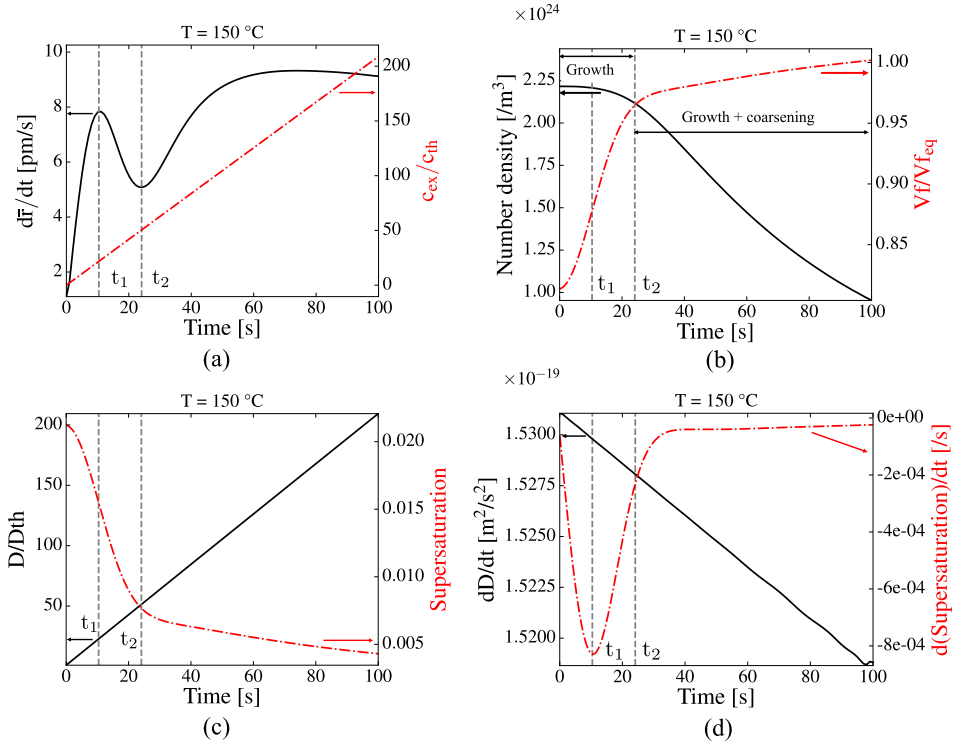

Fig. 8. (a) Evolution of growth rate (plain line) and excess vacancies (dotted line) as a function of time. (b) Evolution of precipitate number density (plain line) and relative volume fraction (dotted line) as a function of time. (c) Evolution of D_{th}/D (plain line) and supersaturation (dotted line) as a function of time. (d) Time evolution of the derivative with respect to time of diffusion coefficient (plain line) and supersaturation (dotted line). All calculations are made for deformation with $\dot{\epsilon} = 10^{-2}$ s^{-1}.

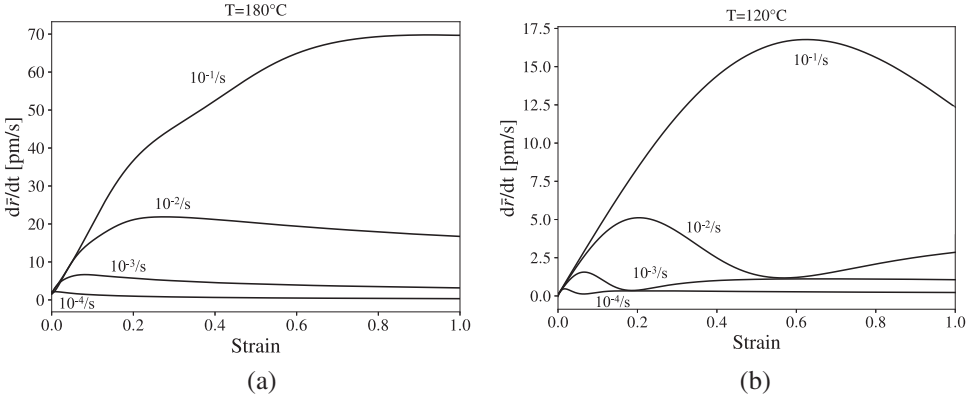

Fig. 9. Evolution of the calculated growth rate with respect to time as a function of strain at (a) 120 °C and (b) 180 °C.

Table 3
Input parameters used to calibrate the model.

Symbol	Parameter	Value
T	Temperature	160 °C
s	Dispersion parameter	0.25
r_0	Initial mean radius	1.85 nm
v_f^0/v_f^{eq} (160 °C)	Initial precipitate volume fraction compared to equilibrium	0.82
L	Grain size	50 μm
ρ	Dislocation density	10^{14} m^{-2}
$\dot{\epsilon}(t)$	Strain rate	graph in Deschamps et al. [3]

cipitate state. This is illustrated in Fig. 10 at two different temperatures for the initial state given in Table 3. It is emphasised that this type of processing map is strongly dependent on the initial distribution and thus on the applied pre-ageing treatment. It can be seen from Fig. 10 that for the conditions examined here, the necessary time to reach a certain precipitate radius is always reduced when the strain or strain rate increases. Additionally, for a given level of deformation, the precipitate radius reached at the end of the deformation decreases when the strain rate increases, which is due to the fact that, for a given level of strain, a higher strain rate allows less time for precipitate growth and coarsening to take place compared to a lower strain rate.

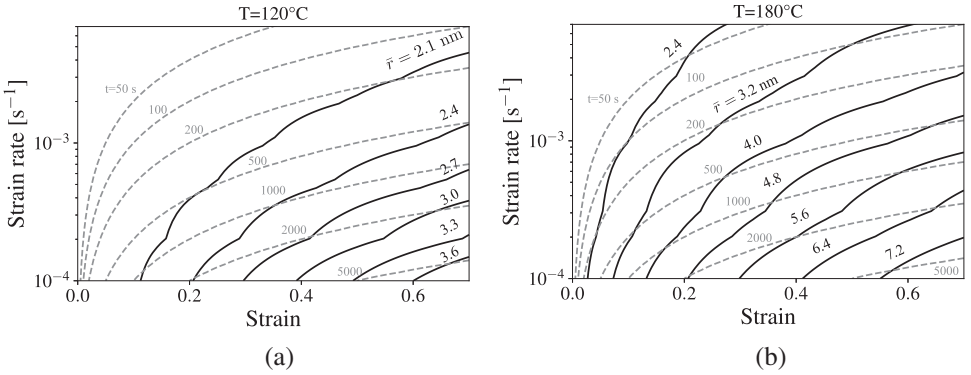

Fig. 10. Processing maps for dynamic precipitation at (a) 120 °C, (b) 180 °C. The plain lines show the iso-values for the mean radius $\bar{r}$ as a function of strain and strain rate, while the dotted lines show the deformation duration corresponding to the process conditions. The calculations are made for the initial distribution described in Table 3, where the initial mean radius is equal to 1.85 nm.

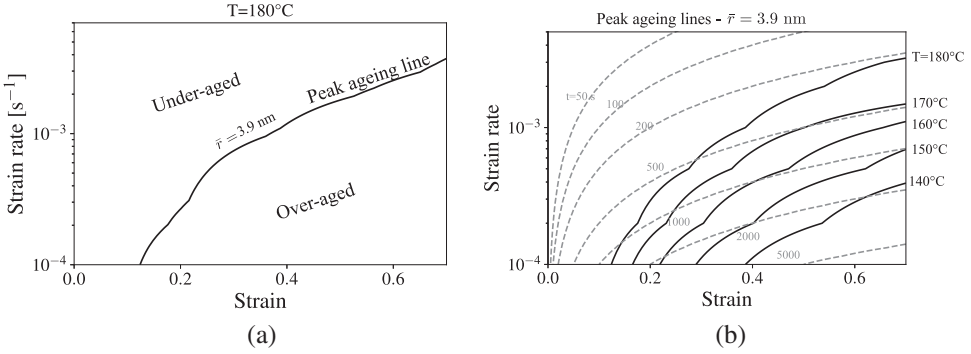

Fig. 11. (a) Processing map showing the combinations of strain level and strain rate leading to peak ageing at 180 °C, along with the regions corresponding to under-ageing and over-ageing. (b) Processing map showing the combinations of strain level and strain rate leading to peak ageing for different temperatures (plain lines), along with the deformation duration corresponding to these conditions (dotted lines).

The mechanical properties in age-hardened aluminium alloys depend on the precipitate distribution and could therefore be estimated as a function of the processing conditions using for instance the model of Deschamps et al. [51]. Although the calculation of the mechanical properties - that continuously vary as the deformation proceeds - is out of the scope of the present work, the dynamic precipitation model can be used to estimate the deformation conditions necessary to reach peak ageing. Assuming that peak-ageing corresponds to a mean radius of 3.3 nm [52], the processing maps of Fig. 10 provide the combinations of strain and strain rate leading to under-ageing, peak-ageing or overageing, as schematically illustrated in Fig. 11(a) for 180 °C. The mean radius isolines, presented for instance in Fig. 10, can then be used to determine the deformation conditions leading to peak ageing for different temperatures, as shown in Fig. 11(b).

4.4. Influence of dislocation density

4.4.1. Time evolution of the dislocation density

The annihilation rate of excess vacancies is proportional to the density of forest dislocations. It has been assumed here that the dislocation density has already reached its saturation value and is constant. To evaluate the influence of this simplifying assumption, a dynamically evolving dislocation density was introduced into the model. A well established semi-empirical dislocation evolution law was used that describes the evolution of the forest dislocation density from an initial (ρ_0) to a steady state (ρ_s) as [27]:

$$\rho(\epsilon) = \rho_s \cdot \left[1 - \frac{\sqrt{\rho_s} - \sqrt{\rho_0}}{\sqrt{\rho_s}} \cdot \exp\left(\frac{c}{2}\epsilon\right)\right]^2 \tag{16}$$

where c is an empirical constant taken as 0.86 for aluminium [27]. In this law, the dislocation density evolution is considered as insensitive to temperature, which, as a first approximation, should be reasonable for the limited range of temperatures considered here (100 to 200 °C) [27].

Fig. 12 shows the effect of including a varying dislocation density in the model, considering a slow strain rate of $\dot{\epsilon} = 10^{-5}$/s and a relatively high temperature of 180 °C, where predictions are most sensitive to this parameter. The saturation dislocation density ρ_s is considered to be 10^{14} m^{-2} [50] - the influence of this value will be discussed later, and ρ_0 is taken as 10^{10} m^{-2} - as for well annealed alloys [37]. The initial distribution parameters are the same as in Table 3. As shown in Fig. 12(a), the initial dislocation density is lower in the early stages of deformation when considering an evolving dislocation density. When the forest dislocation density is low, the annihilation rate is reduced, and this means that the resultant excess vacancies concentration initially increases faster in the evolving dislocation density case, until the steady state is established. However, the difference in the excess vacancies concentrations between the steady state and evolving dislocation density model are always quite small, and decrease with increasing time. Furthermore, the difference is greatest during the initial stages of deformation where the concentration of excess vacancies is smallest and thus the growth rate enhancement effect is least. As a result, the predicted evolution in precipitate radius (Fig. 12(c)) is very similar when comparing the case of an evolving and a steady state dislocation density. Since accounting for the evolving dislocation density introduces further complexity and calibration parameters in the model but does not significantly affect the important outputs (the evolution of precipitate size), it can be reasonably ignored, at least for the range of conditions considered here.

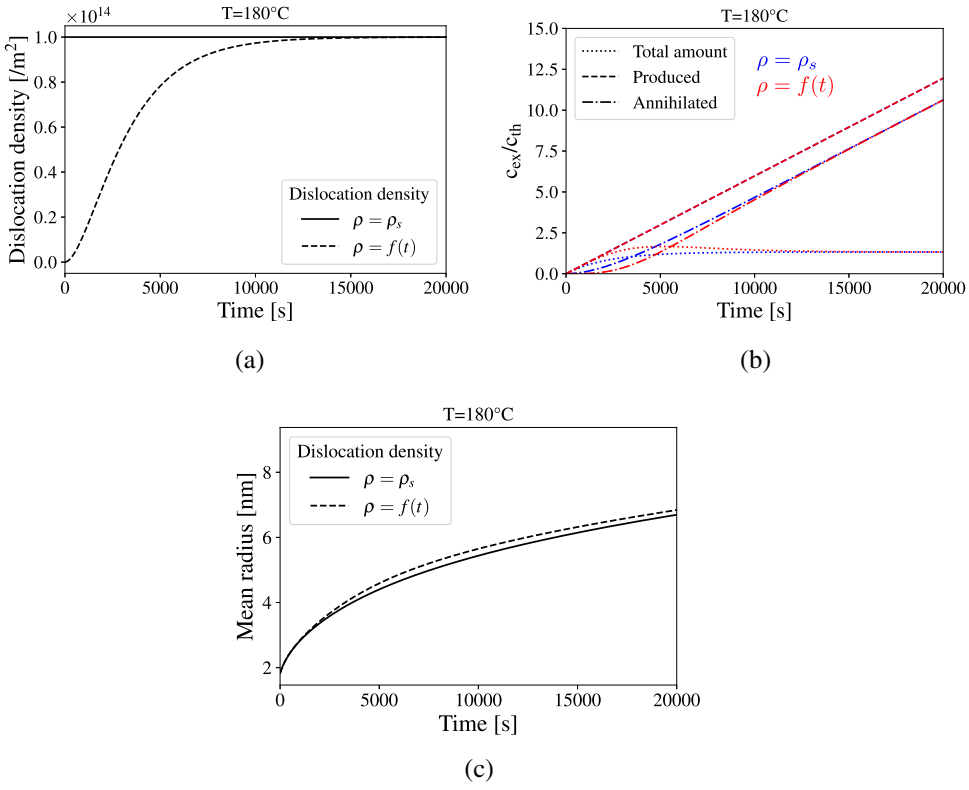

Fig. 12. Evolution of (a) the dislocation density, (b) the amount of excess vacancies, and (c) the mean radius as a function of time, considering a constant dislocation density equal to 10^{14} m^{-2} (blue curves) or a dislocation density varying from 10^{10} to 10^{14} m^{-2} following the law given in Eq. (16). The calculations are made for 180 °C and $\dot{\epsilon} = 10^{-5}$/s. (For interpretation of the references to colour in this figure legend, the reader is referred to the web version of this article.)

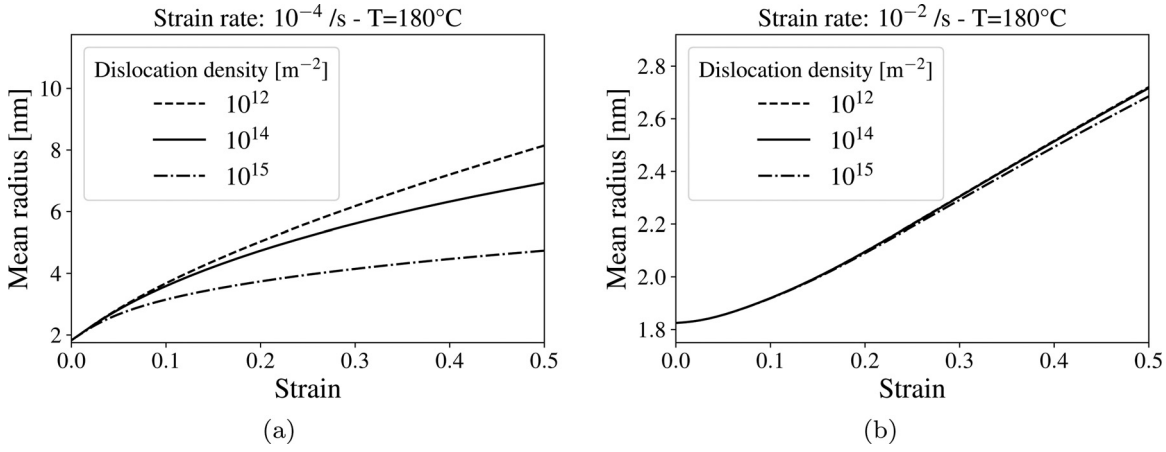

Fig. 13. Evolution of the mean radius as a function of strain for different dislocation density saturations, at 180 °C and (a) $\dot{\epsilon} = 10^{-4}$/s or (b) $\dot{\epsilon} = 10^{-2}$/s.

4.4.2. Value of the saturation dislocation density

The saturation value of the dislocation density, assumed here to be equal to 10^{14} m^{-2} is not very well defined. In the literature, estimated or measured values of ρ_s are usually around 10^{14} m^{-2} for aluminium alloys and vary between 2×10^{12} and 10^{15} m^{-2} [3,53–55]. Fig. 13 shows the effect of changing the dislocation density saturation to the extremum values of 10^{12} and 10^{15} m^{-2} compared to the reference value of 10^{14} m^{-2} adopted in this work, at lower and higher strain rates (10^{-4} and 10^{-2} /s, respectively). The calculations are made at relatively high temperature (180 °C), where the effect of changing the dislocation density is expected to be greatest due to more rapid excess vacancies annihilation. The initial distribution is the same as in Table 3. Fig. 13 shows that the evolution of the radius is sensitive to the dislocation density at low strain rate but not at high strain rate, which is expected because the annihilation of vacancies at dislocations is a time-dependent process. At sufficiently high strain rates, there is insufficient time for significant excess vacancies annihilation during deformation regardless of the sink density (within a reasonable range).

5. Conclusions

The coupling between deformation and precipitation has been investigated by integrating the effect of excess vacancies formation in a KWN growth and coarsening kinetics framework for a multicomponent aluminium alloy. The precipitation growth rate and size distribution evolution have been calculated over a large range of strains and strain rates (10^{-5} to 1 s^{-1}) at temperatures between

100 °C and 200 °C. The following conclusions can be drawn from this work:

1. The acceleration of precipitation growth and coarsening due to deformation can be predicted combining the KWN model and a classical phenomenological model for excess vacancies formation, as demonstrated with experimental data from the literature.
2. For all process parameters explored here, deformation leads to an enhancement in precipitation rate compared to static ageing during an equivalent time, and this enhancement is highest for relatively low temperatures and high strain rates.
3. As opposed to static precipitation in a supersaturated matrix, where the growth rate continuously decreases with time, the precipitate growth rate calculated under deformation may continuously increase (relatively low temperature, high strain rate), continuously decrease (higher temperature, low strain rate), or exhibit a mixture of both types of behaviour resulting in one or several maxima (intermediate strain rate and temperatures).
4. The sensitivity of precipitation growth rate to strain and strain rate may be positive or negative depending on the ranges of conditions considered.

Data statement

All data presented here is available from the LightForm community in the Zenodo repository: 10.5281/zenodo.6090249.

Declaration of Competing Interest

The authors declare that they have no known competing financial interests or personal relationships that could have appeared to influence the work reported in this paper.

Acknowledgements

The authors are grateful to the EPSRC for financial support through the associated programme grant LightFORM (EP/R001715/1). JDR would like to acknowledge financial support through the DSTL/RAEng Chair in Alloys for Extreme Environments. MB would like to acknowledge Ziyu Ma for useful discussions.

References

[1] M. Cai, D.P. Field, G.W. Lorimer, A systematic comparison of static and dynamic ageing of two Al-Mg-Si alloys, Mater. Sci. Eng. A 373 (1–2) (2004) 65–71, doi:10.1016/j.msea.2003.12.035.
[2] K. Teichmann, C.D. Marioara, K.O. Pedersen, K. Marthinsen, The effect of simultaneous deformation and annealing on the precipitation behaviour and mechanical properties of an Al-Mg-Si alloy, Mater. Sci. Eng. A 565 (2013) 228–235, doi:10.1016/j.msea.2012.12.042.
[3] A. Deschamps, G. Fribourg, Y. Bréchet, J.L. Chemin, C.R. Hutchinson, In situ evaluation of dynamic precipitation during plastic straining of an Al-Zn-Mg-Cu alloy, Acta Mater. 60 (5) (2012) 1905–1916, doi:10.1016/j.actamat.2012.01.002.
[4] C.R. Hutchinson, F. De Geuser, Y. Chen, A. Deschamps, Quantitative measurements of dynamic precipitation during fatigue of an Al-Zn-Mg-(Cu) alloy using small-angle X-ray scattering, Acta Mater. 74 (2014) 96–109, doi:10.1016/j.actamat.2014.04.027.
[5] L. Couturier, A. Deschamps, F. De Geuser, F. Fazeli, W.J. Poole, An investigation of the strain dependence of dynamic precipitation in an Al-Zn-Mg-Cu alloy, Scr. Mater. 136 (2017) 120–123, doi:10.1016/j.scriptamat.2017.04.031.
[6] W. Sun, Y. Zhu, R. Marceau, L. Wang, Q. Zhang, X. Gao, C. Hutchinson, Precipitation strengthening of aluminum alloys by room-temperature cyclic plasticity, Science 363 (6430) (2019) 972–975, doi:10.1126/science.aav7086.
[7] W.U. Mirihanage, J.D. Robson, S. Mishra, P. Hidalgo-Manrique, J. Quinta da Fonseca, C.S. Daniel, P.B. Prangnell, S. Michalik, O.V. Magdysyuk, T. Connolley, M. Drakopoulos, Direct observation of the dynamic evolution of precipitates in aluminium alloy 7021 at high strain rates via high energy synchrotron X-rays, Acta Mater. 205 (2021) 116532, doi:10.1016/j.actamat.2020.116532.
[8] W. Huo, L. Hou, Y. Zhang, J. Zhang, Warm formability and post-forming microstructure/property of high-strength AA 7075-T6 Al alloy, Mater. Sci. Eng. A 675 (2016) 44–54, doi:10.1016/j.msea.2016.08.054.
[9] M. Kumar, N.G. Ross, Influence of temper on the performance of a high-strength Al-Zn-Mg alloy sheet in the warm forming processing chain, J. Mater. Process. Technol. 231 (2016) 189–198, doi:10.1016/j.jmatprotec.2015.12.026.
[10] A. Deschamps, F. Bley, F. Livet, D. Fabregue, L. David, In-situ small-angle X-ray scattering study of dynamic precipitation in an Al-Zn-Mg-Cu alloy, Philos. Mag. 83 (6) (2003) 677–692, doi:10.1080/0141861021000051091.
[11] H.J. Roven, M. Liu, J.C. Werenskiold, Dynamic precipitation during severe plastic deformation of an Al-Mg-Si aluminium alloy, Mater. Sci. Eng. A 483–484 (1–2C) (2008) 54–58, doi:10.1016/j.msea.2006.09.142.
[12] J.D. Embury, A. Deschamps, Y. Brechet, The interaction of plasticity and diffusion controlled precipitation reactions, Scr. Mater. 49 (2003) 927–932, doi:10.1016/S1359-6462(03)00479-2. 10 SPEC
[13] J.D. Robson, M.J. Jones, P.B. Prangnell, Extension of the N-model to predict competing homogeneous and heterogeneous precipitation in Al-Sc alloys, Acta Mater. 51 (5) (2003) 1453–1468, doi:10.1016/S1359-6454(02)00540-2.
[14] G.R. Love, Dislocation pipe diffusion, Acta Metall. 12 (1964) 731–737.
[15] A.L. Ruoff, R.W. Balluffi, On strain-enhanced diffusion in metals. III. Interpretation of recent experiments, J. Appl. Phys. 34 (9) (1963) 2862–2872, doi:10.1063/1.1729822.
[16] J.D. Robson, Deformation enhanced diffusion in aluminium alloys, Metall. Mater. Trans. A 51 (10) (2020) 5401–5413, doi:10.1007/s11661-020-05960-5.
[17] M. Nicolas, A. Deschamps, Characterisation and modelling of precipitate evolution in an Al-Zn-Mg alloy during non-isothermal heat treatments, Acta Mater. 51 (20) (2003) 6077–6094, doi:10.1016/S1359-6454(03)00429-4.
[18] R. Wagner, R. Kampmann, P.W. Voorhees, Homogeneous second-phase precipitation, in: Phase Transform. Mater., 2005, pp. 309–407, doi:10.1002/352760264x.ch5.
[19] D. Zhao, Y. Xu, S. Gouttebroze, J. Friis, Y. Li, Modelling the age-hardening precipitation by a revised langer and schwartz approach with log-normal size distribution, Metall. Mater. Trans. A 51 (9) (2020) 4838–4852, doi:10.1007/s11661-020-05879-x.
[20] A. Simar, Y. Bréchet, B. de Meester, A. Denquin, T. Pardoen, Sequential modeling of local precipitation, strength and strain hardening in friction stir welds of an aluminum alloy 6005A-T6, Acta Mater. 55 (18) (2007) 6133–6143, doi:10.1016/j.actamat.2007.07.012.
[21] D.A. Porter, K.E. Easterling, K.E. Easterling, Phase transformations in metals and alloys (revised reprint), Phase Transform. Met. Alloy. (Revised Repr.) (2009), doi:10.1201/9781439883570.
[22] D. Bardel, M. Perez, D. Nelias, A. Deschamps, C.R. Hutchinson, D. Maisonnette, T. Chaise, J. Garnier, F. Bourlier, Coupled precipitation and yield strength modelling for non-isothermal treatments of a 6061 aluminium alloy, Acta Mater. 62 (1) (2014) 129–140, doi:10.1016/j.actamat.2013.09.041.
[23] A. Deschamps, C.R. Hutchinson, Precipitation kinetics in metallic alloys: experiments and modeling, Acta Mater. 220 (2021) 117338, doi:10.1016/j.actamat.2021.117338.
[24] C.G. Lenasson, A semi-phenomenological expression for the strain dependence of vacancy concentration during plastic deformation, Scr. Metall. 6 (12) (1972) 1125–1128, doi:10.1016/0036-9748(72)90216-5.
[25] H. Mecking, Y. Estrin, The effect of vacancy generation on plastic deformation, Scr. Metall. 14 (7) (1980) 815–819, doi:10.1016/0036-9748(80)90295-1.
[26] M. Militzer, W.P. Sun, J.J. Jonas, Modelling the effect of deformation-induced vacancies on segregation and precipitation, Acta Metall. Mater. 42 (1) (1994) 133–141, doi:10.1016/0956-7151(94)90056-6.
[27] K. Detemple, O. Kanert, J.T.M. De Hosson, K.L. Murty, In situ nuclear magnetic resonance investigation of deformation-generated vacancies in aluminium, Phys. Rev. B 52 (1) (1995) 125–133.
[28] K. Linga Murty, K. Detemple, O. Kanert, J.T.M. Dehosson, In-situ nuclear magnetic resonance investigation of strain, temperature, and strain-rate variations of deformation-induced vacancy concentration in aluminum, Metall. Mater. Trans. A 29 (1) (1998) 153–159, doi:10.1007/s11661-998-0168-0.
[29] F.D. Fischer, J. Svoboda, F. Appel, E. Kozeschnik, Modeling of excess vacancy annihilation at different types of sinks, Acta Mater. 59 (9) (2011) 3463–3472, doi:10.1016/j.actamat.2011.02.020.
[30] M.J. Zehetbauer, G. Steiner, E. Schafler, A.V. Korznikov, E. Korznikova, Deformation induced vacancies with severe plastic deformation: measurements and modelling, Mater. Sci. Forum 503–504 (2006) 57–64. www.scientific.net/msf.503-504.57
[31] M. Perez, M. Dumont, D. Acevedo-Reyes, Implementation of classical nucleation and growth theories for precipitation, Acta Mater. 56 (9) (2008) 2119–2132, doi:10.1016/j.actamat.2007.12.050.
[32] J.D. Robson, Modelling the overlap of nucleation, growth and coarsening during precipitation, Acta Mater. 52 (15) (2004) 4669–4676, doi:10.1016/j.actamat.2004.06.024.
[33] S.K. Maloney, K. Hono, I.J. Polmear, S.P. Ringer, The chemistry of precipitates in an aged Al-2.1Zn-1.7Mg at.% alloy, Scr. Mater. 41 (10) (1999) 1031–1038, doi:10.1016/S1359-6462(99)00253-5.
[34] M. Dumont, W. Lefebvre, B. Doisneau-Cottignies, A. Deschamps, Characterisation of the composition and volume fraction of η and η' precipitates in an Al-Zn-Mg alloy by a combination of atom probe, small-angle X-ray scattering and transmission electron microscopy, Acta Mater. 53 (10) (2005) 2881–2892, doi:10.1016/j.actamat.2005.03.004.
[35] A. Deschamps, F. De Geuser, On the validity of simple precipitate size measurements by small-angle scattering in metallic systems, J. Appl. Crystallogr. 44 (2) (2011) 343–352, doi:10.1107/S0021889811003049.
[36] M. Perez, Gibbs–Thomson effects in phase transformations, Scr. Mater. 52 (8) (2005) 709–712, doi:10.1016/j.scriptamat.2004.12.026.

[37] D. Hull, D.J. Bacon, Introduction to dislocations, Introduction to Dislocations, 2011, doi:10.1016/C2009-0-64358-0.
[38] H. Wang, P. Colegrove, H.M. Mayer, L. Campbell, R.D. Robson, Material constitutive behaviour and microstructure study on aluminium alloys for friction stir welding, Adv. Mater. Res. 89–91 (2010) 615–620. www.scientific.net/AMR.89-91.615
[39] J. Bass, The formation and motion energies of vacancies in aluminium, Philos. Mag. 15 (136) (1967) 717–730, doi:10.1080/14786436708220919.
[40] J.D. Embury, R.B. Nicholson, The nucleation of precipitates: the system Al-Zn-Mg, Acta Metall. 13 (4) (1965) 403–417, doi:10.1016/0001-6160(65)90067-2.
[41] Y. Du, Y.A. Chang, B. Huang, W. Gong, Z. Jin, H. Xu, Z. Yuan, Y. Liu, Y. He, F.Y. Xie, Diffusion coefficients of some solutes in fcc and liquid Al: critical evaluation and correlation, Mater. Sci. Eng. A 363 (1–2) (2003) 140–151, doi:10.1016/S0921-5093(03)00624-5.
[42] S. Nenno, J.W. Kauffman, Detection of equilibrium vacancy concentrations in aluminium, Philos. Mag. 4 (48) (1959) 1382–1384, doi:10.1080/14786435908233375.
[43] P. Tzanetakis, J. Hillairet, G. Revel, The formation energy of vacancies in aluminium and magnesium, Phys. Status Solidi 75 (2) (1976) 433–439, doi:10.1002/pssb.2220750205.
[44] J. Herrnring, B. Sundman, P. Staron, B. Klusemann, Modeling precipitation kinetics for multi-phase and multi-component systems using particle size distributions via a moving grid technique, Acta Mater. 215 (2021) 117053, doi:10.1016/j.actamat.2021.117053.
[45] N. Kamp, A. Sullivan, J.D. Robson, Modelling of friction stir welding of 7xxx aluminium alloys, Mater. Sci. Eng. A 466 (1–2) (2007) 246–255, doi:10.1016/j.msea.2007.02.070.
[46] X.W. Nie, L.J. Zhang, Y. Du, Experiments and modeling of double-peak precipitation hardening and strengthening mechanisms in Al-Zn-Mg alloy, Trans. Nonferrous Met. Soc. China (English Ed.) 24 (7) (2014) 2138–2144, doi:10.1016/S1003-6326(14)63324-0.
[47] P. Schloth, Precipitation in the High Strength AA7449 Aluminium Alloy, École Polytechnique Fédérale de Lausanne, 2015 Ph.D. thesis.
[48] C. Liu, A. Davis, J. Fellowes, P.B. Prangnell, D. Raabe, P. Shanthraj, CALPHAD-informed phase-field model for two-sublattice phases based on chemical potentials: η-phase precipitation in Al-Zn-Mg-Cu alloys, Acta Mater. 226 (2022) 117602, doi:10.1016/j.actamat.2021.117602.
[49] G. Fribourg, A. Deschamps, Y. Bréchet, Precipitation strengthening in AA7449 aluminium alloy: understanding the relationship between microstructure, yield strength and strain hardening, Mater. Sci. Forum 519–521 (2006) 991–996. www.scientific.net/msf.519-521.991
[50] G.K. Williamson, R.E. Smallman III, Dislocation densities in some annealed and cold-worked metals from measurements on the X-ray Debye–Scherrer spectrum, Philos. Mag. 1 (1) (1956) 34–46, doi:10.1080/14786435608238074.
[51] A. Deschamps, Y. Brechet, Influence of predeformation and ageing of an Al-Zn-Mg Alloy-II. Modeling of precipitation kinetics and yield stress, Acta Mater. 47 (1) (1998) 293–305, doi:10.1016/S1359-6454(98)00296-1.
[52] G. Fribourg, Y. Bréchet, A. Deschamps, A. Simar, Microstructure-based modelling of isotropic and kinematic strain hardening in a precipitation-hardened aluminium alloy, Acta Mater. 59 (9) (2011) 3621–3635, doi:10.1016/j.actamat.2011.02.035.
[53] J. Gubicza, N.Q. Chinh, Z. Horita, T.G. Langdon, Effect of Mg addition on microstructure and mechanical properties of aluminum, Mater. Sci. Eng. A 387–389 (2004) 55–59, doi:10.1016/j.msea.2004.03.076. 1–2 SPEC. ISS
[54] A. Pesin, A. Korchunov, D. Pustovoytov, Numerical study of grain evolution and dislocation density during asymmetric rolling of aluminum alloy 7075, Key Eng. Mater. 685 (2016) 162–166. scientific.net/KEM.685.162
[55] L. Oger, B. Malard, G. Odemer, L. Peguet, C. Blanc, Influence of dislocations on hydrogen diffusion and trapping in an Al-Zn-Mg aluminium alloy, Mater. Des. 180 (2019) 107901, doi:10.1016/j.matdes.2019.107901.